



Short-term global horizontal irradiance forecasting based on a hybrid CNN-LSTM model with spatiotemporal correlations

Haixiang Zang^{a,*}, Ling Liu^a, Li Sun^b, Lilin Cheng^a, Zhinong Wei^a, Guoqiang Sun^a

^a College of Energy and Electrical Engineering, Hohai University, Nanjing, 210098, China

^b College of Energy and Environment, Southeast University, Nanjing, 210096, China

ARTICLE INFO

Article history:

Received 27 November 2019

Received in revised form

26 May 2020

Accepted 27 May 2020

Available online 26 June 2020

Keywords:

Solar irradiance

CNN

LSTM

Spatiotemporal correlation

ABSTRACT

Accurate short-term solar irradiance forecasting is crucial for ensuring the optimum utilization of photovoltaic power generation sources. This study addresses this issue by proposing a spatiotemporal correlation model based on deep learning. The proposed model first applies a convolutional neural network (CNN) to extract spatial features from a two-dimensional matrix composed of meteorological parameters associated with a target site and its neighboring sites. Then, a long short-term memory (LSTM) network is applied to extract temporal features from historical solar irradiance time-series data associated with the target site. Finally, the spatiotemporal correlations are merged to predict global horizontal irradiance one hour in advance. The prediction performance and generalization ability of the proposed CNN-LSTM model are evaluated within a whole year, under diverse seasons and sky conditions. Three datasets are involved for case studies, which are collected from 34 locations spread across three different climate zones in Texas, USA. Moreover, the performance of the CNN-LSTM model is compared with those obtained using the CNN, LSTM, and other benchmark models based on five evaluation metrics. The results indicate that the proposed model has advantages over the other models considered and provides a good alternative for short-term solar radiation prediction.

© 2020 Elsevier Ltd. All rights reserved.

1. Introduction

The rapid development of the global economy has increasingly relied on fossil fuels such as oil and coal, resulting in heavy environmental pollution and greenhouse effects [1]. Hence, the exploitation of renewable energy sources has generated increasing interest in pursuit of environmental protection worldwide [2]. Among these energy sources, solar energy represents one of the most promising options, particularly its use in photovoltaic (PV) power generation [3]. However, solar irradiance can be heavily influenced by rapid changes in cloud conditions, and is therefore stochastic in nature [4]. This variability can have a substantial impact on power grid security when connected with large scale PV generation. Therefore, developing accurate short-term solar irradiance forecasting models is crucial for ensuring the optimum dispatch and management of power systems, particularly with increasing penetration of PV power generation [5].

A considerable amount of research has been devoted to

developing solar irradiance forecasting models. From the literature, these forecasting models can be divided into four main categories based on the input data adopted [6–9]: (1) numerical weather prediction (NWP) models based on atmospheric data [10–12]; (2) image-based models [13]; (3) statistical models based on historical data [14,15]; (4) hybrid models based on multiple types of input data [16–19].

Local cloud cover information is inferred by NWP models through the dynamic modeling of the atmosphere [20]. This method has been widely used for solar radiation forecasting 6–48h ahead [21]. However, this approach is typically ill-suited for conducting short-term solar irradiance prediction due to the high calculation costs involved [22]. In addition, NWP models do not readily capture real-time temporal relationships between solar irradiance and meteorological factors, which further limits their short-term solar irradiance prediction capabilities [23].

Unlike NWP models, image-based models directly capture cloud cover information from satellite or ground-based sky images for conducting solar irradiance forecasting. The high spatial and temporal resolutions of satellite and ground-based images facilitate the detailed tracking of cloud motion [6,21]. As such, image-based

* Corresponding author.

E-mail address: zanghaixiang@hhu.edu.cn (H. Zang).

Nomenclature

ARMA	auto-regressive moving average	PSM	physical solar model
ANN	artificial neural network	PW	precipitable water (cm)
BSh	hot semi-arid climate	RMSE	root mean square error (W/m ²)
BSk	cold semi-arid climate	RH	relative humidity (%)
CNN	convolutional neural network	ReLU	rectified linear unit
CARDS	coupled autoregressive and dynamical system	RNN	recurrent neural network
Cfa	humid subtropical climate	R	correlation coefficient
DPT	dew point temperature (°C)	SVM	support vector machine
GHI	global horizontal irradiance (W/m ²)	SZA	solar zenith angle (degrees)
LSTM	long short-term memory	T	temperature (°C)
ML	machine learning	WS	wind speed (m/s)
MAE	mean absolute error (W/m ²)	WD	wind direction (degrees)
MSE	mean square error	2D	two-dimensional
NWP	numerical weather prediction	μ	mean value of the global horizontal irradiance (W/m ²)
nMAE	normalized MAE (%)	S	number of sites
nRMSE	normalized RMSE (%)	F	number of meteorological parameters
PV	photovoltaic	k_t	clearness index

models provide an effective solar irradiance forecast horizon ranging from minutes to several hours in advance [13,24]. Nevertheless, the high cost of image capture facilities limits the widespread use of image-based models.

In contrast to the previous two models, statistical models are based on historical solar irradiance data, and are usually applied to forecasting timescales ranging from 5 min up to 6 h [6,25,26]. Typical examples of statistical models include the auto-regressive moving average (ARMA) model [14] and the coupled autoregressive and dynamical system (CARDS) model [15]. The ARMA model is a good choice for predicting the future values of a specific solar irradiance time series, but the time series must be stationary. The CARDS model has been demonstrated over the past several decades to capture the linear relationships between historical data and future irradiance values accurately [26]. However, the CARDS model fails to capture complex nonlinear relationships accurately, which can greatly detract from its prediction performance when these conditions arise in historical data.

Although statistical models are often a good choice for conducting solar irradiance forecasting based on time series data, they can only consider historical data, and other relevant weather conditions affecting solar irradiance cannot be included within the forecasting process. This shortcoming can be overcome by integrating different types of input data in hybrid models via machine learning (ML) approaches. ML approaches possess the advantage of extracting complex nonlinear features from multiple inputs [27]. A number of ML models, such as artificial neural network (ANN) [28–30] and support vector machine (SVM) [29], have been widely used in solar radiation forecasting due to their relatively good performance when employed with small data sample sizes. In Ref. [29], ANN and SVM are adopted for 1h-ahead solar radiation forecasting, which possess root mean square error (RMSE) values ranging 84.21 W/m² ~ 124.77 W/m² and 85.36 W/m² ~ 123.33 W/m², respectively. However, conventional ML models can only extract shallow features, and usually require complex feature engineering operations [23].

This issue associated with conventional ML models has been addressed in recent years by the development of deep learning, such as convolutional neural network (CNN) and long short-term memory (LSTM) network, that rely on the representation learning of data [31]. Deep learning models improve the accuracy of classification or prediction by using deep nonlinear network structures

to realize complex function approximation, as well as by the use of deep features from massive samples [32–38]. These models can extract features spontaneously through multiple stacked hidden layers, and therefore alleviate the need for complex feature engineering operations. For example, the application of an LSTM network to solar irradiance forecasting based on historical time series data was demonstrated to obtain good prediction performance [36]. In addition, the superiority of CNN for extracting spatial correlations was demonstrated by adopting a CNN to extract cloud cover features [39]. With an increasing amount of spatiotemporal-correlated data, solar radiation prediction requires further research with a comprehensive consideration of spatiotemporal correlation.

Meanwhile, although CNN and LSTM have been widely studied for solar radiation prediction, they are mainly designed for spatial and temporal computations, respectively. Researches should be further carried out on the rational combinations of the two state-of-the-art models, in order to fully integrate their respective merits [23]. Motivated by this, the present study proposes a hybrid CNN-LSTM model that seeks to take full advantages of the superiority of CNN for extracting spatial features and the superiority of LSTM network for extracting time-series features to improve the accuracy of global horizontal irradiance (GHI) prediction. The main contributions of the present study are given as follows.

- (1) Meteorological parameters and historical solar irradiance are innovatively reconstructed to better extract spatiotemporal features. First, the meteorological parameters of a target site and its surrounding sites are reconstructed into a two-dimensional (2D) matrix to extract spatial features. Then, historical irradiance time-series data associated with the target site are reconstructed to extract temporal features.
- (2) The CNN and LSTM models are innovatively integrated into a new CNN-LSTM model. The hybrid CNN-LSTM model combines spatial and temporal correlations by merging the spatial features extracted by the CNN and the temporal features extracted by the LSTM network. Then, the GHI is predicted 1 h in advance through the dense layer of the hybrid network structure.
- (3) The prediction performance and generalization ability of the CNN-LSTM model are rigorously evaluated by analyzing the prediction results in a whole year, different seasons and sky

conditions when applied to three datasets composed of spatiotemporal data collected from 34 locations spread across three different climate zones. Meanwhile, the CNN-LSTM model is compared with seven benchmark methods based on five evaluation metrics.

The remainder of this paper is organized as follows. Section 2 introduces the datasets used in this study. Section 3 describes the working principles of the basic networks used in the present study in detail. Section 4 presents the processing flow of the proposed hybrid CNN-LSTM model, the process employed for performance evaluation, and the performance evaluation metrics used in the process. In Section 5, we present results and discussions related to the model performance evaluation based on the datasets introduced in Section 2 in comparison with other benchmark models. Finally, Section 6 summarizes the information presented in this article and proposes future work.

2. Datasets

The details for each of the 34 locations in Texas, USA are listed in Table 1. These details include the humid subtropical climate (Cfa), hot semi-arid climate (BSh), and cold semi-arid climate (BSk) climate zones [40], latitude, longitude and the statistical mean value (μ) of the GHI at each location based on physical solar model (PSM) data obtained from the National Solar Radiation Data Base developed by the National Renewable Energy Laboratory [21,41]. Additional data for each location include the hourly GHI, dew point temperature (DPT), solar zenith angle (SZA), wind speed (WS), wind direction (WD), precipitable water (PW), relative humidity

(RH), and temperature (T) observed from January 1, 2006 to December 31, 2012. Because the GHI drops to zero at night, only data observed from 6:00 to 18:00 per day are selected for training and testing. The data of each climate zone constitute a dataset and each dataset is divided into a training set comprising data ranging from January 1, 2006 to December 31, 2011 and a testing set comprising data ranging from January 1, 2012 to December 31, 2012. The target site is randomly selected from all the sites in a given dataset. Multiple target sites are selected within a dataset. When a target site is selected, the rest of the sites in the dataset are neighboring sites. Each testing only targets at one target site (i.e., only solar radiation of this target site are predicted). The target sites selected for each dataset are marked in bold and the number of values and the percents corresponding to each training and testing sets are also given in Table 1.

3. Principles of basic methods

3.1. Convolutional neural network

A CNN is a feedforward neural network proposed by LeCun [42]. As shown in Fig. 1, the architecture of a typical CNN consists of a convolutional layer, pooling layer, and fully connected layer [43]. In essence, a CNN seeks to construct multiple filters capable of extracting hidden features through a layer-by-layer convolution and pooling of input data. Finally, these abstract features are merged through the fully connected layer, and an activation function is used to solve the classification or regression problem.

In the convolution layer, feature maps of the previous layer are convolved with a convolution kernel and the output feature maps

Table 1
Geographic parameters and solar irradiance datasets of the 34 locations in Texas, USA employed in the present study.

Dataset	Location	Latitude (N)	Longitude (E)	μ (W/m ²)	Training period	Testing period
1 (Cfa)	Liberty	30°29'	−94°94'	368.87	28483 (86%)	4758 (14%)
	Dallas	32°93'	−97°02'	384.24	28483 (86%)	4758 (14%)
	Shackelford	32°77'	−99°38'	398.87	28483 (86%)	4758 (14%)
	Nacogdoches	31°77'	−94°74'	371.68	28483 (86%)	4758 (14%)
	Burnet	30°65'	−98°34'	390.57	28483 (86%)	4758 (14%)
	Bee	28°41'	−97°86'	387.15	28483 (86%)	4758 (14%)
	Baylor	33°73'	−99°34'	393.56	28483 (86%)	4758 (14%)
	Jack	33°29'	−98°38'	390.23	28483 (86%)	4758 (14%)
	Dewitt	29°13'	−97°06'	380.66	28483 (86%)	4758 (14%)
	Rains	32°89'	−95°94'	367.45	28483 (86%)	4758 (14%)
	San Jacinto	30°81'	−95°26'	370.45	28483 (86%)	4758 (14%)
	Goliad	28°57'	−97°70'	384.61	28483 (86%)	4758 (14%)
2 (BSh)	Upton	31°49'	−102°26'	437.59	28483 (86%)	4758 (14%)
	Pecos	31°09'	−102°62'	441.56	28483 (86%)	4758 (14%)
	Terrell	30°13'	−101°98'	431.97	28483 (86%)	4758 (14%)
	Val Verde	29°65'	−101°02'	407.40	28483 (86%)	4758 (14%)
	Reagan	31°13'	−101°34'	402.22	28483 (86%)	4758 (14%)
	Kinney	29°09'	−100°42'	399.78	28483 (86%)	4758 (14%)
	Zapata	26°89'	−99°02'	411.36	28483 (86%)	4758 (14%)
	Crockett	31°05'	−101°70'	426.02	28483 (86%)	4758 (14%)
3 (BSk)	Dallam	36°29'	−102°54'	410.50	28483 (86%)	4758 (14%)
	Sherman	36°29'	−101°66'	403.50	28483 (86%)	4758 (14%)
	Ochiltree	36°25'	−100°62'	396.09	28483 (86%)	4758 (14%)
	Hartley	35°93'	−102°54'	414.95	28483 (86%)	4758 (14%)
	Moore	35°85'	−101°66'	406.71	28483 (86%)	4758 (14%)
	Oldham	35°45'	−102°74'	416.75	28483 (86%)	4758 (14%)
	Carson	35°33'	−101°58'	411.33	28483 (86%)	4758 (14%)
	Wheeler	35°41'	−100°46'	400.66	28483 (86%)	4758 (14%)
	Randall	34°93'	−101°78'	414.10	28483 (86%)	4758 (14%)
	Collingsworth	34°93'	−100°50'	406.10	28483 (86%)	4758 (14%)
	Lamb	34°13'	−102°22'	422.83	28483 (86%)	4758 (14%)
	Briscoe	34°33'	−101°14'	408.81	28483 (86%)	4758 (14%)
	Cottle	34°25'	−100°14'	399.15	28483 (86%)	4758 (14%)
	Martin	32°09'	−101°90'	410.86	28483 (86%)	4758 (14%)

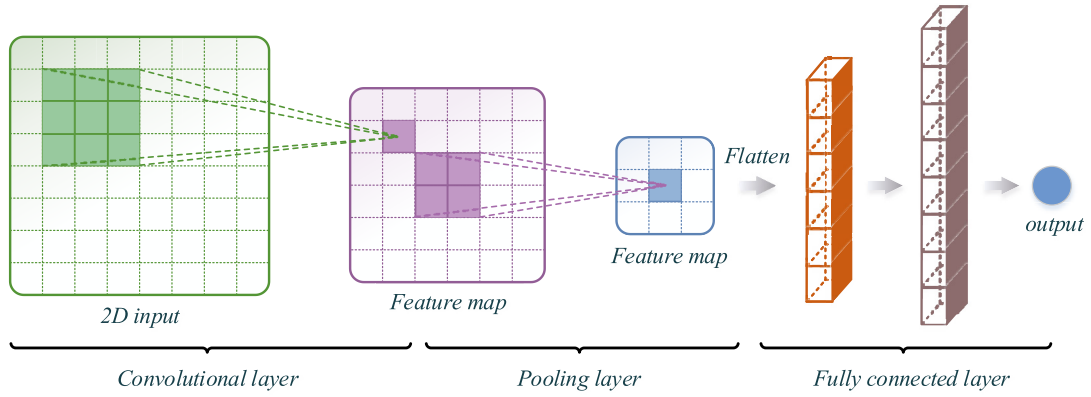


Fig. 1. Basic architecture of a CNN.

are generated by an activation function. The operation of the convolutional layer can be depicted as follows [44]:

$$x_j^l = f \left(\sum_{i \in M_j} x_i^{l-1} * k_{ij}^l + b_j^l \right), \quad (1)$$

where x_j^l represents the j th output feature map of the l th layer, x_i^{l-1} represents the i th output feature map of the $(l-1)$ th layer, M_j represents the selection of input maps, k_{ij}^l represents the weights between the i th input map and the j th output map, $*$ represents the convolution operation, b_j^l represents the bias, and $f(\cdot)$ represents the rectified linear unit (ReLU) activation function.

The pooling layer is employed to reduce the number of CNN parameters. This is realized by calculating the average (average pooling) or maximum (maximum pooling) value of a given area in a feature map. The operation of the pooling layer can be depicted as follows:

$$x_j^l = f \left(\beta_j^l \text{down}(x_j^{l-1}) + b_j^l \right), \quad (2)$$

where $\text{down}(\cdot)$ represents the maxpooling subsampling function, x_j^{l-1} represents the j th input feature map of the l th layer, and β_j^l is the bias.

Finally, the feature maps obtained by calculations of multiple convolutional and pooling layers are taken as the inputs of the fully connected layer, which then calculates the final output vector as follows:

$$x^l = f \left(K^l x^{l-1} + b^l \right), \quad (3)$$

where x^l represents the final output vector, x^{l-1} represents the input vector, K^l represents the weights between the $(l-1)$ th layer and the l th layer, and b^l represents the bias.

3.2. Long short-term memory network

An LSTM network is an enhanced recurrent neural network (RNN) that has the ability to automatically store and remove temporal state information. This ability solves the gradient disappearance problem of the RNN in dealing with long-term sequences and facilitates the extraction of complex time-series features [45]. As shown in Fig. 2, a complete LSTM network contains an input gate, output gate, and forget gate.

The operations of the forget gate f_t , input gate i_t , and output gate o_t at time step t can be depicted respectively as follows [36,46].

$$f_t = \sigma(W_f \cdot [h_{t-1}, x_t] + b_f) \quad (4)$$

$$i_t = \sigma(W_i \cdot [h_{t-1}, x_t] + b_i) \quad (5)$$

$$o_t = \sigma(W_o \cdot [h_{t-1}, x_t] + b_o) \quad (6)$$

here, x_t denotes the input at time step t , h_{t-1} denotes the output at time step $t-1$, W_f , W_i , and W_o denote the weight matrices of the forget gate, input gate, and output gate, respectively, b_f , b_i , and b_o are the biases of the forget gate, input gate, and output gate, respectively, and $\sigma(\cdot)$ is the sigmoid activation function. The final output of an LSTM network h_t is jointly determined by o_t and the memory cell state c_t at t . The relevant calculations are as follows.

$$\tilde{c}_t = \tanh(W_c \cdot [h_{t-1}, x_t] + b_c) \quad (7)$$

$$c_t = c_{t-1} * f_t + i_t * \tilde{c}_t \quad (8)$$

$$h_t = o_t * \tanh(c_t) \quad (9)$$

here, $\tanh(\cdot)$ denotes the tanh activation function, W_c denotes the weight matrix of the memory cell, b_c denotes the bias of the memory cell, and \tilde{c}_t denotes the temporary memory cell state at t .

4. Processing flow of the proposed hybrid model and its evaluation process

The processing flow of the proposed GHI prediction method based on the hybrid CNN-LSTM model is illustrated in Fig. 3(1) and (2), while the process employed for evaluating its prediction performance is illustrated in Fig. 3(3). Input dimension reconstruction is first conducted to better extract spatial and temporal features (Fig. 3(1)). The hourly meteorological parameters of all sites are reconstructed (i.e., input 1) to obtain spatial features, while the historical irradiance data of the target site are reconstructed (i.e., input 2) to obtain temporal features. Inputs 1 and 2 are then used as the inputs of the proposed hybrid CNN-LSTM model to predict the GHI of each target site 1 h in advance (Fig. 3(2)). The three datasets corresponding to the three climate zones are employed for evaluating the performances of the CNN-LSTM, persistence model, SVM, ANN, CNN, LSTM, CNN-ANN, and ANN-LSTM in terms of year, seasons and sky conditions based on the mean absolute error (MAE),

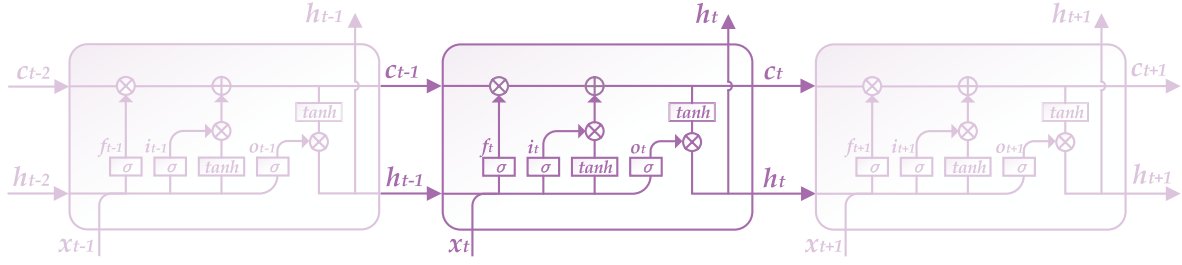


Fig. 2. Basic architecture of an LSTM network.

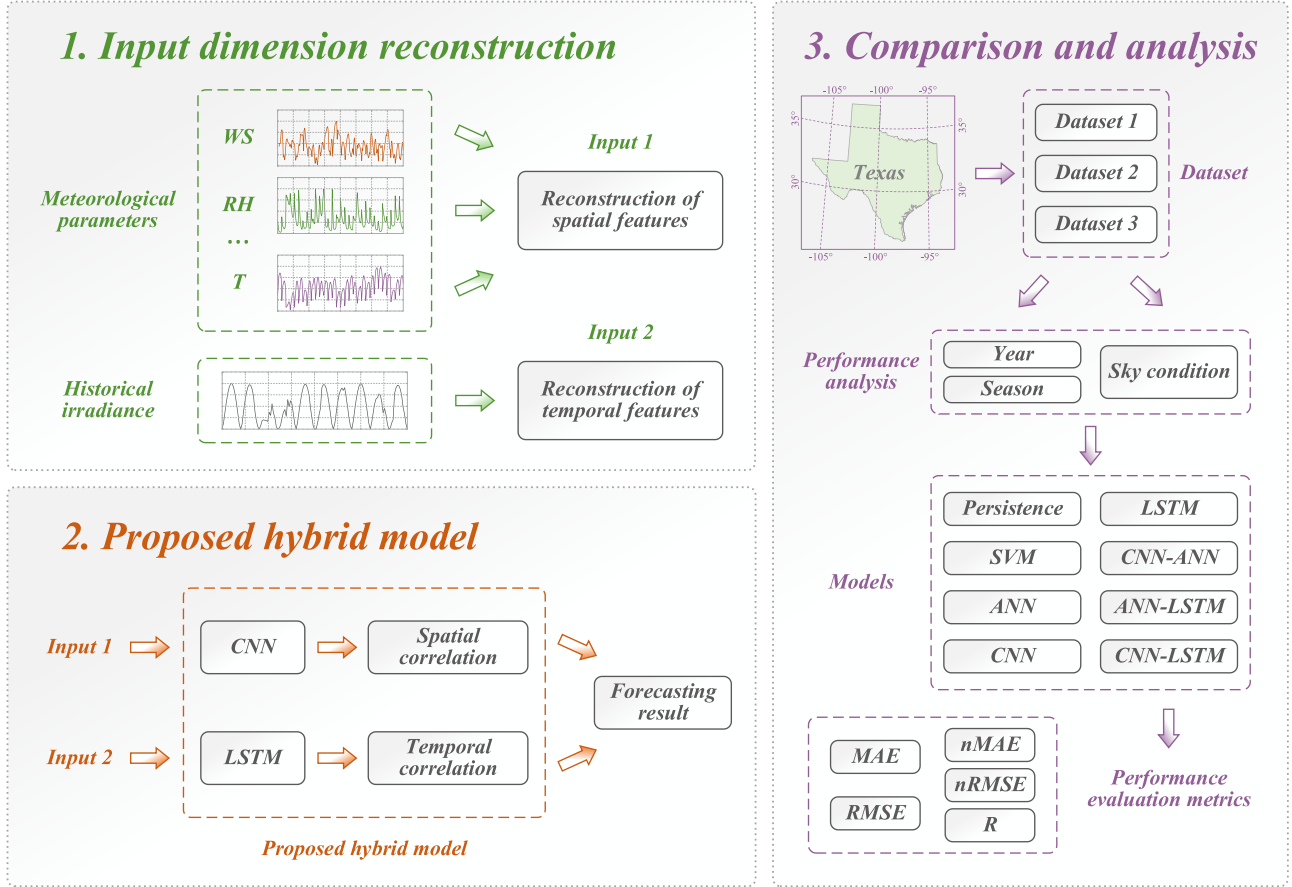


Fig. 3. Flow chart of the proposed GHI prediction method based on the hybrid CNN-LSTM model and the process employed for evaluating its prediction performance.

normalized MAE (nMAE), RMSE, normalized RMSE (nRMSE) and correlation coefficient (R) (Fig. 3(3)). The details regarding each of these processes are discussed in the following subsections.

4.1. Input dimension reconstruction

4.1.1. Reconstruction of spatial features

In the spatial reconstruction process, all meteorological parameters of the target site and neighboring sites at the target time t are formed into a 2D matrix, as illustrated in Fig. 4, which is then used to extract the spatial correlations between sites. Here, each row contains all meteorological parameters of a given site at the target time, and each column contains the same meteorological parameters for all sites. Accordingly, the 2D matrix is composed of elements $f_{i,j}$ ($i = 1, 2, \dots, S$ and $j = 1, 2, \dots, F$), where S represents the number of sites and F represents the number of meteorological

parameters. As shown in Fig. 4, a given meteorological parameter exhibits correlations between different sites, which are specifically manifested in the correlations between two adjacent elements in the same column. This site correlation $corr_1$ is defined as follows:

$$corr_1 = g(f_{i,j}, f_{i+1,j}), \quad (10)$$

where $g(\cdot)$ represents the pearson correlation function. Meanwhile, correlations also exist between different meteorological parameters for the same site, which is specifically manifested in the correlations between two adjacent elements in the same row. This parameter correlation $corr_2$ is defined as follows:

$$corr_2 = g(f_{i,j}, f_{i,j+1}), \quad (11)$$

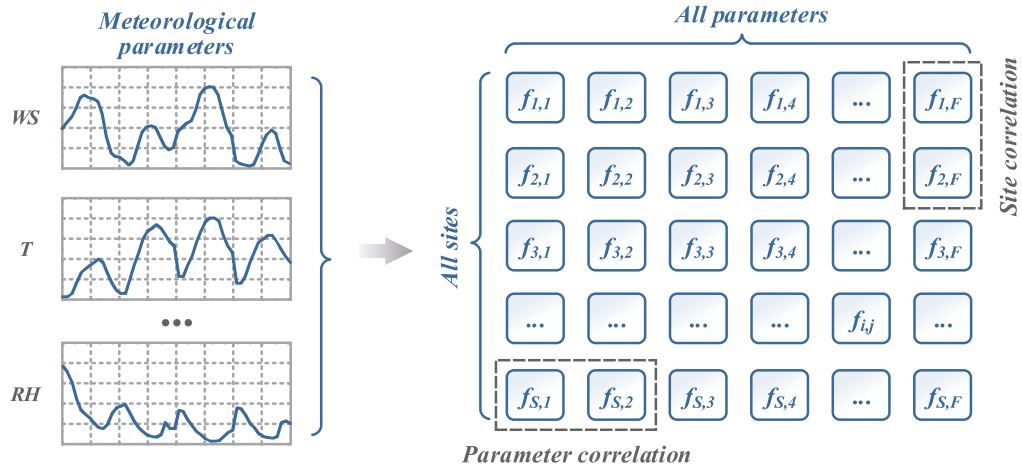


Fig. 4. Spatial feature reconstruction process for input 1 of the proposed hybrid model.

4.1.2. Reconstruction of temporal features

In the temporal reconstruction process illustrated in Fig. 5, the historical GHI sequence x_i ($i = 1, 2, \dots$) for a given target site is a discrete time series, and each hour corresponds to a time step, as shown by the purple circles in the figure, which represent the GHI distribution over time. The GHI values of each time step are sequentially sent to a single LSTM unit (see Subsection 3.2). The connected LSTM units on the right represent the expansion of the leftmost LSTM unit in the time domain and y_i ($i = 1, 2, \dots$) represents the output of each time step. Accordingly, the status of each LSTM unit is updated at each time step. In this study, the GHI values of the previous 10 h are taken as the inputs of the LSTM network (i.e., the LSTM unit holds this information in memory) to predict the GHI 1 h in advance. This construction fully reveals the implied temporal correlations in historical GHI sequences.

4.2. Proposed hybrid model

The structure of the proposed hybrid CNN-LSTM model for combining the spatial and temporal correlations is illustrated in Fig. 6. All meteorological parameters DPT, SZA, WS, WD, PW, RH, and T of the target site and neighboring sites at the target time step t (obtained by weather forecast) are reconstructed as the input 1, the historical irradiance values of the target site from time step $t-10$ to $t-1$ are reconstructed as the input 2, and the output is the GHI of the target site at time step t . The hybrid model is divided into spatiotemporal feature extraction, which merges the spatial features extracted by the CNN from input 1 and the temporal features extracted by the LSTM from input 2 via a concatenation operation, and GHI prediction in the final fully connected layer. The benchmark models CNN-ANN and ANN-LSTM for comparison replace LSTM and CNN with ANN, respectively. The inputs and outputs of

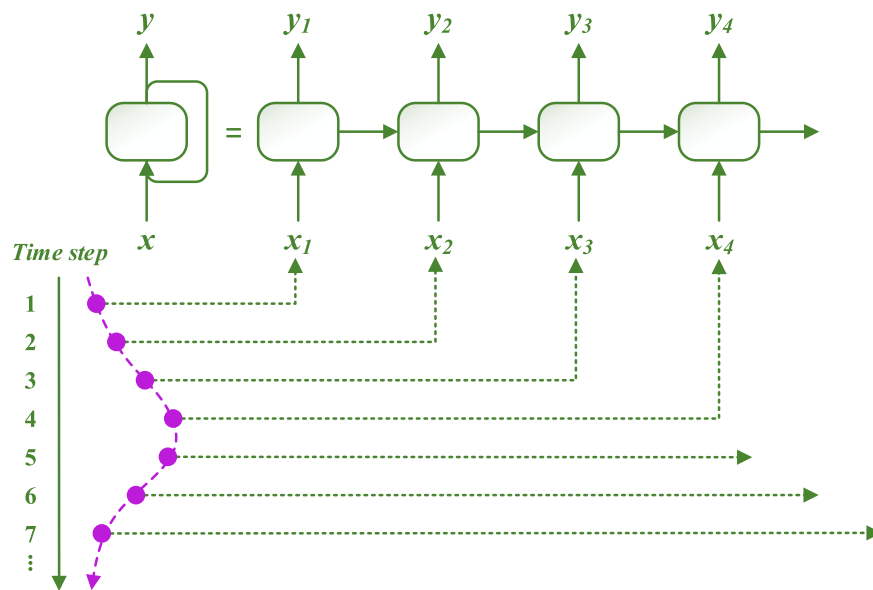


Fig. 5. Temporal feature reconstruction process for input 2 of the proposed hybrid model.

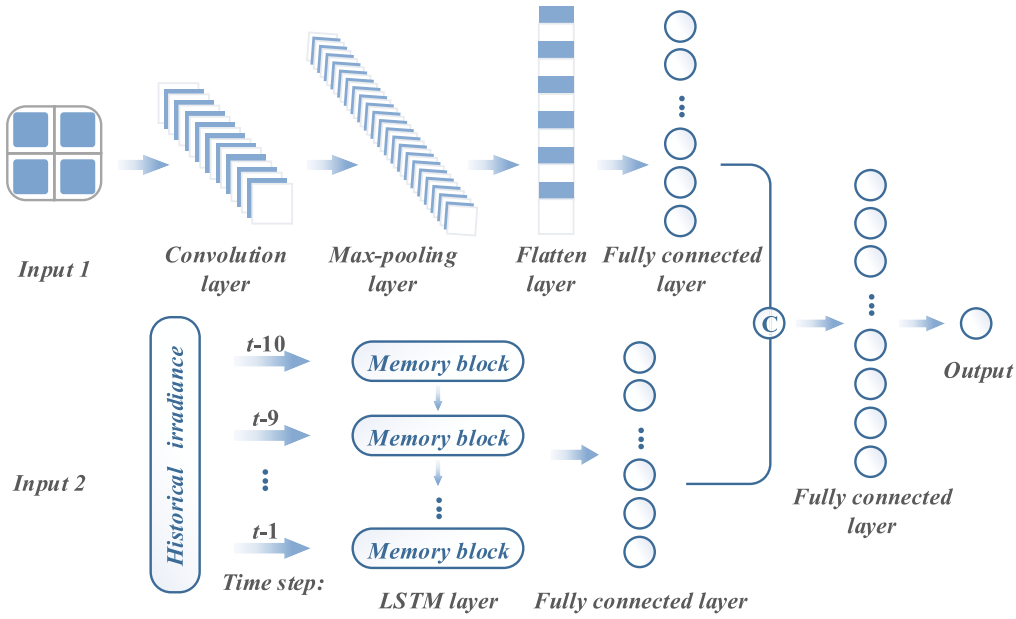


Fig. 6. Structure of the proposed hybrid CNN-LSTM model.

CNN-ANN, ANN-LSTM, SVM and ANN are the same as those of CNN-LSTM (i.e., the inputs are meteorological parameters and historical irradiance, the output is the forecasted GHI of the target site). The difference is that the data are directly input to the ANN parts of CNN-ANN and ANN-LSTM, SVM and ANN without reconstruction. The CNN model only considers spatial correlation and takes input 1 as input. The LSTM model only considers temporal correlation and takes input 2 as input. The persistence model supposes that the GHI value at the target time t is best predicted by its previous value at time $t-1$. The outputs of CNN, LSTM and persistence model are also the same as that of CNN-LSTM.

4.3. Performance evaluation metrics

No standard presently exists for conducting model performance evaluation, which increases the difficulty of model comparison. Therefore, the present work adopts five performance evaluation metrics, including the MAE, nMAE, RMSE, nRMSE, and R , to evaluate the prediction performances of the models adequately. These metrics are computed as follows [47].

$$\text{MAE} = \frac{1}{N} \times \sum_{i=1}^N |\hat{y}_i - y_i| \quad (12)$$

$$\text{nMAE} = \frac{\frac{1}{N} \times \sum_{i=1}^N |\hat{y}_i - y_i|}{y_a} \times 100\% \quad (13)$$

$$\text{RMSE} = \sqrt{\frac{1}{N} \times \sum_{i=1}^N (\hat{y}_i - y_i)^2} \quad (14)$$

$$\text{nRMSE} = \frac{\sqrt{\frac{1}{N} \times \sum_{i=1}^N (\hat{y}_i - y_i)^2}}{y_a} \times 100\% \quad (15)$$

$$R = \frac{\left| \sum_{i=1}^N (\hat{y}_i - \hat{y}_a) \cdot (y_i - y_a) \right|}{\sqrt{\left[\sum_{i=1}^N (\hat{y}_i - \hat{y}_a)^2 \right] \left[\sum_{i=1}^N (y_i - y_a)^2 \right]}} \quad (16)$$

here, \hat{y}_i and y_i represent the i th forecasted and measured values, respectively. \hat{y}_a and y_a are the averaged forecasted and measured values, respectively. N is the total number of observations. The prediction performance of a given model increases with decreasing values of MAE, nMAE, RMSE and nRMSE and increasing values of R .

5. Results and discussion

The performance of the proposed GHI prediction method is analyzed for each target site of the three datasets listed in Table 1 within a whole year, under diverse seasons and sky conditions. The proposed hybrid model is built in Python using Keras, which is a deep learning library that is capable of running on TensorFlow, Theano, and CNTK. Fairness in the testing results is ensured by employing equivalent parameters for all models in each experiment. The models use Adam optimizer to optimize parameters and mean square error (MSE) as the loss function. Each model uses early stopping with the number of iterations set to 100. The initial learning rate and batch size are set to 0.001 and 512, respectively. All experiments are conducted on a personal computer equipped with the Windows 7 operating system, 8.00 GB RAM, and an Intel® Core™ i5-6400 CPU operating at 2.70 GHz.

5.1. Annual performance

The evaluation metric values obtained for annual prediction testing of the eight models at the five target sites considered (i.e., Dallas, San Jacinto, Zapata, Moore, and Lamb) are listed in Table 2. The values given in bold represent the best values obtained for all models. In addition, the MAE values obtained for the CNN-LSTM model at all target sites are compared with those of the other models in Fig. 7, while this is presented in terms of the RMSE in Fig. 8. Finally, the percentile improvements in all annual

Table 2

Annual prediction results of different models for the three datasets listed in Table 1.

Metric	Model	Cfa		BSh	BSk	
		Dallas	San Jacinto	Zapata	Moore	Lamb
MAE (W/m ²)	Persistence model	119.80	123.05	127.91	122.00	126.24
	SVM	65.43	72.00	67.34	60.79	61.42
	ANN	46.78	54.77	47.19	43.73	40.85
	CNN	55.75	66.86	59.52	52.15	52.29
	LSTM	46.71	57.54	48.75	41.03	40.01
	CNN-ANN	43.22	54.29	44.52	38.28	37.87
	ANN-LSTM	43.99	54.21	45.58	38.00	37.85
	CNN-LSTM	41.88	52.00	43.66	37.26	37.20
nMAE (%)	Persistence model	30.27	32.57	30.76	29.20	29.34
	SVM	16.53	19.06	16.19	14.55	14.28
	ANN	11.82	14.50	11.35	10.47	9.49
	CNN	14.09	17.69	14.31	12.48	12.15
	LSTM	11.80	15.23	11.72	9.82	9.30
	CNN-ANN	10.92	14.37	10.71	9.16	8.80
	ANN-LSTM	11.12	14.35	10.96	9.10	8.80
	CNN-LSTM	10.58	13.76	10.50	8.92	8.65
RMSE (W/m ²)	Persistence model	149.81	153.67	158.14	149.41	153.74
	SVM	87.94	96.27	90.26	81.28	83.64
	ANN	80.12	86.83	80.65	72.25	72.95
	CNN	97.10	104.37	97.86	90.42	95.43
	LSTM	82.86	91.93	83.55	74.28	75.49
	CNN-ANN	78.45	87.36	79.04	69.75	71.83
	ANN-LSTM	77.45	86.66	79.98	69.94	71.84
	CNN-LSTM	78.17	86.33	78.49	69.26	71.61
nRMSE (%)	Persistence model	37.86	40.67	38.03	35.76	35.74
	SVM	22.22	25.48	21.70	19.46	19.44
	ANN	20.24	22.98	19.39	17.29	16.96
	CNN	24.53	27.62	23.53	21.64	22.18
	LSTM	20.94	24.33	20.09	17.78	17.55
	CNN-ANN	19.82	23.12	19.01	16.69	16.70
	ANN-LSTM	19.57	22.93	19.23	16.74	16.70
	CNN-LSTM	19.75	22.85	18.87	16.58	16.65
R	Persistence model	0.8797	0.8654	0.8747	0.8864	0.8827
	SVM	0.9600	0.9471	0.9597	0.9676	0.9665
	ANN	0.9650	0.9561	0.9669	0.9732	0.9733
	CNN	0.9482	0.9361	0.9510	0.9575	0.9541
	LSTM	0.9625	0.9506	0.9644	0.9715	0.9713
	CNN-ANN	0.9665	0.9555	0.9683	0.9749	0.9741
	ANN-LSTM	0.9673	0.9563	0.9676	0.9748	0.9741
	CNN-LSTM	0.9667	0.9566	0.9688	0.9753	0.9742

performance metrics obtained by the proposed model relative to those of the other models at the different target sites are listed in Table 3.

According to Table 2, the annual prediction performance of the CNN-LSTM model is best for all datasets in terms of the MAE and nMAE. In addition, the annual prediction performance of the proposed model is best for all datasets in terms of the RMSE, nRMSE and R, except for the Dallas target site, where the ANN-LSTM model provides slightly better prediction results.

The improved annual prediction performances obtained by the proposed model relative to the other models at all target sites are intuitively obvious from the MAE and RMSE data respectively presented in Figs. 7 and 8, while the specific improvements are listed in Table 3. According to the figures and tables, the performance improvement of CNN-LSTM is the biggest compared with the persistence model with percentile improvements in the R ranging from 9.89% to 10.76%. The annual performance of the CNN-LSTM model is substantially better than those obtained by the SVM and ANN models, demonstrating the superiority of the proposed model over conventional machine learning models. This is particularly the case when compared with the prediction results of the SVM model. Taking the MAE as an example, we note that the values

of this performance metric obtained by the CNN-LSTM model are decreased in percentiles ranging from 27.78% to 39.43% when compared with SVM. However, when compared with ANN, the percentile performance increases of the CNN-LSTM model range from 5.06% to 14.80%. Moreover, the proposed hybrid CNN-LSTM model also yields prediction results that are far superior to those of the CNN model, which only considers spatial correlations, with percentile improvements in the MAE ranging from 22.23% to 28.86%, while improvements relative to the results of the LSTM model, which only considers temporal correlations, are much more modest (i.e., percentile improvements ranging from 7.02% to 10.44%). When compared with results obtained from the hybrid CNN-ANN and ANN-LSTM models, the increased performance of the proposed hybrid CNN-LSTM model is not so obvious. In terms of the nMAE, the percentile performance increase of the CNN-LSTM model ranges from 1.70% to 4.24% when compared with the CNN-ANN model and from 1.70% to 4.86% when compared with the ANN-LSTM model. Although the prediction performance of the CNN-LSTM model is not the best in three of the 25 total cases (i.e., five target sites and five evaluation metrics), the proposed model is still the best choice overall, demonstrating the superiority of the CNN-LSTM combination strategy.

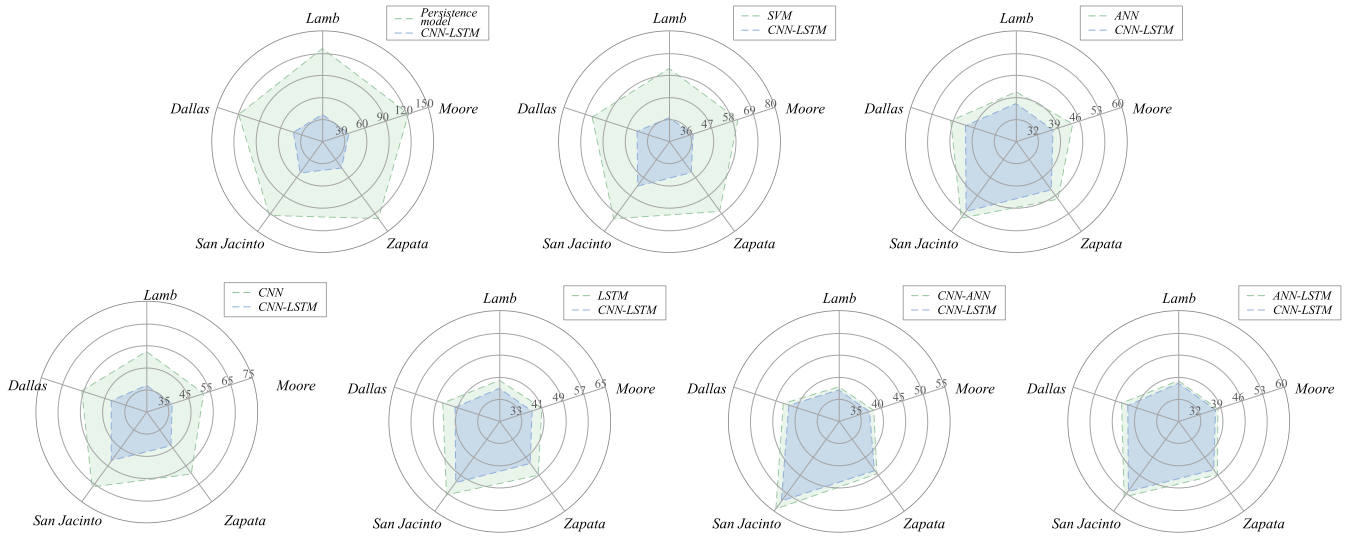


Fig. 7. Comparison of the annual prediction results of the CNN-LSTM model and those of the other models in terms of the MAE.

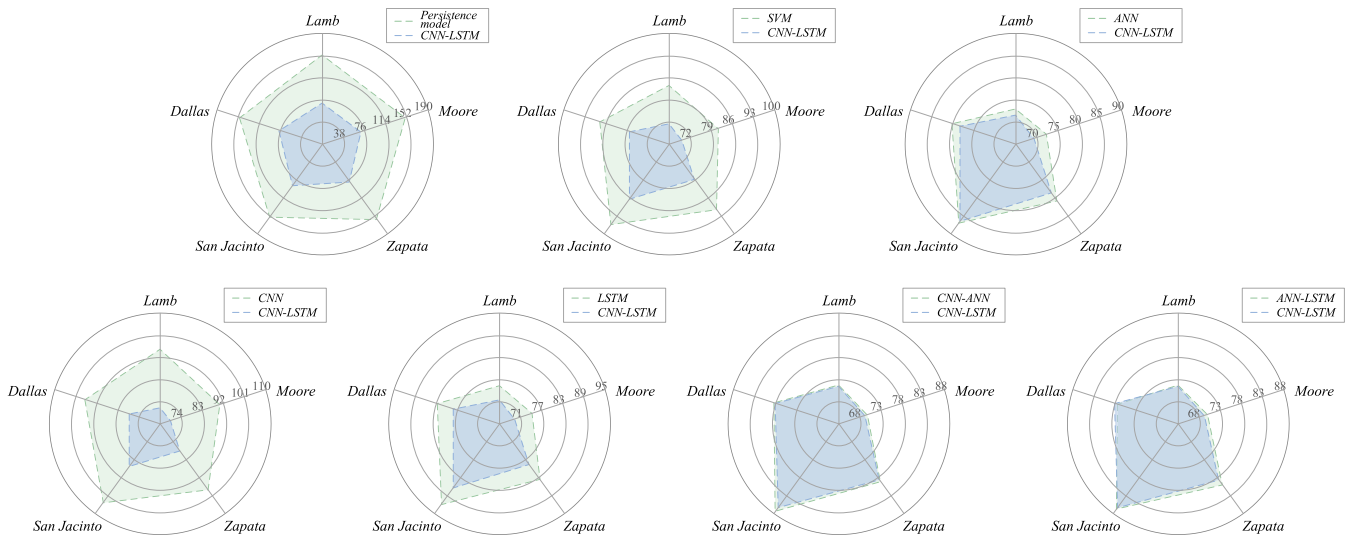


Fig. 8. Comparison of the annual prediction results of the CNN-LSTM model and those of the other models in terms of the RMSE.

5.2. Seasonal performance

The seasonal prediction performance results for the eight models at the five target sites considered are listed in Table 4, where the values given in bold represent the best performance evaluation metric values of all models. In addition, the results in Table 4 for the normalized evaluation metrics are replicated graphically in Fig. 9 along with the seasonal GHI distribution curves for each of the five target sites. The normalized metrics are applied in the figure to facilitate comparisons between the seasonal results because the MAE and RMSE values differ for different seasons owing to differences in solar intensity. According to the prediction results listed in Table 4, the proposed hybrid CNN-LSTM model achieves the best prediction performance in most cases, regardless of the season. We also note from the GHI distribution curves in Fig. 9 that the curve predicted by the CNN-LSTM model is generally closer to the actual values than those curves obtained from the other models. Nevertheless, we note that the prediction performance of the CNN-LSTM model varies from season to season

depending on the target site considered.

The results in Table 4 and Fig. 9 indicate that the normalized prediction errors for the Dallas and San Jacinto target sites are smaller in spring and summer, slightly greater in autumn, and greatest in winter. The results for the two sites are similar because Dallas and San Jacinto are both in the Cfa climate zone. A comprehensive analysis of the nMAE and nRMSE results for these target sites indicates that the prediction performance of the CNN-LSTM model is more greatly improved relative to the performances of the other models in autumn and winter, but less so in the other two seasons. Taking the Dallas target site as an example, the nMAE value obtained by the CNN-LSTM model in winter is less than those obtained by the persistence model, SVM, ANN, CNN, LSTM, CNN-ANN, and ANN-LSTM models by 21.35%, 7.09%, 1.92%, 4.81%, 2.36%, 0.60%, and 0.86%, respectively. However, the nMAE value obtained by the CNN-LSTM model in spring, where performance improvements are not so obvious, is less than those obtained by the persistence model, SVM, ANN, CNN, LSTM, CNN-ANN, and ANN-LSTM models by 17.24%, 4.55%, 0.76%, 3.38%, 0.77%, 0.43%, and

Table 3

Percentile improvements in the annual performance metrics obtained by the proposed model relative to those of the other models at the different target sites.

Models	Sites	MAE	nMAE	RMSE	nRMSE	R
CNN-LSTM vs Persistence model	Dallas	65.04%	65.05%	47.82%	47.83%	9.89%
	San Jacinto	57.74%	57.75%	43.82%	43.82%	10.54%
	Zapata	65.87%	65.86%	50.37%	50.38%	10.76%
	Moore	69.46%	69.45%	53.64%	53.64%	10.03%
	Lamb	70.53%	70.52%	53.42%	53.41%	10.37%
CNN-LSTM vs SVM	Dallas	35.99%	36.00%	11.11%	11.12%	0.70%
	San Jacinto	27.78%	27.81%	10.33%	10.32%	1.00%
	Zapata	35.16%	35.15%	13.04%	13.04%	0.95%
	Moore	38.71%	38.69%	14.79%	14.80%	0.80%
	Lamb	39.43%	39.43%	14.38%	14.35%	0.80%
CNN-LSTM vs ANN	Dallas	10.47%	10.49%	2.43%	2.42%	0.18%
	San Jacinto	5.06%	5.10%	0.58%	0.57%	0.05%
	Zapata	7.48%	7.49%	2.68%	2.68%	0.20%
	Moore	14.80%	14.80%	4.14%	4.11%	0.22%
	Lamb	8.94%	8.85%	1.84%	1.83%	0.09%
CNN-LSTM vs CNN	Dallas	24.88%	24.91%	19.50%	19.49%	1.95%
	San Jacinto	22.23%	22.22%	17.28%	17.27%	2.19%
	Zapata	26.65%	26.62%	19.79%	19.80%	1.87%
	Moore	28.55%	28.53%	23.40%	23.38%	1.86%
	Lamb	28.86%	28.81%	24.96%	24.93%	2.11%
CNN-LSTM vs LSTM	Dallas	10.34%	10.34%	5.66%	5.68%	0.44%
	San Jacinto	9.63%	9.65%	6.09%	6.08%	0.63%
	Zapata	10.44%	10.41%	6.06%	6.07%	0.46%
	Moore	9.19%	9.16%	6.76%	6.75%	0.39%
	Lamb	7.02%	6.99%	5.14%	5.13%	0.30%
CNN-LSTM vs CNN-ANN	Dallas	3.10%	3.11%	0.36%	0.35%	0.02%
	San Jacinto	4.22%	4.24%	1.18%	1.17%	0.12%
	Zapata	1.93%	1.96%	0.70%	0.74%	0.05%
	Moore	2.66%	2.62%	0.70%	0.66%	0.04%
	Lamb	1.77%	1.70%	0.31%	0.30%	0.01%
CNN-LSTM vs ANN-LSTM	Dallas	4.80%	4.86%	−0.93%	−0.92%	−0.06%
	San Jacinto	4.08%	4.11%	0.38%	0.35%	0.03%
	Zapata	4.21%	4.20%	1.86%	1.87%	0.12%
	Moore	1.95%	1.98%	0.97%	0.96%	0.05%
	Lamb	1.72%	1.70%	0.32%	0.30%	0.01%

0.25%, respectively.

The seasonal trends of the prediction results obtained for the Dallas and San Jacinto target sites differ somewhat for the Zapata target site in the BSh climate zone, where the normalized prediction errors are relatively small in spring and summer, and relatively large in autumn and winter. However, while the normalized prediction errors of the CNN-LSTM model are large in autumn and winter, the performance improvement of the CNN-LSTM model relative to the performances of the other models is greater. For example, the nMAE value obtained by the CNN-LSTM model in spring is reduced by −0.10% compared with that of the CNN-ANN model and 0.04% compared with that of the ANN-LSTM model. However, the nMAE value of the CNN-LSTM model in winter is reduced by 0.49% compared with that of the CNN-ANN model and 0.80% compared with that of the ANN-LSTM model.

In contrast to the Dallas and San Jacinto target sites, the seasonal trends of the prediction results obtained for the Moore and Lamb target sites are different even though both of these sites reside in the BSk climate zone. For Moore, the normalized prediction errors are relatively small in summer and relatively large in winter, while the prediction errors in spring and autumn are similarly in between the values obtained during summer and winter. In addition, the performance improvement of the CNN-LSTM model relative to the performances of the other models varies from season to season, where the proposed model provides the smallest improvement in summer and slightly greater improvement in the other three seasons. Meanwhile, the seasonal prediction error trends for Lamb are similar to those obtained for Dallas and San Jacinto, where the

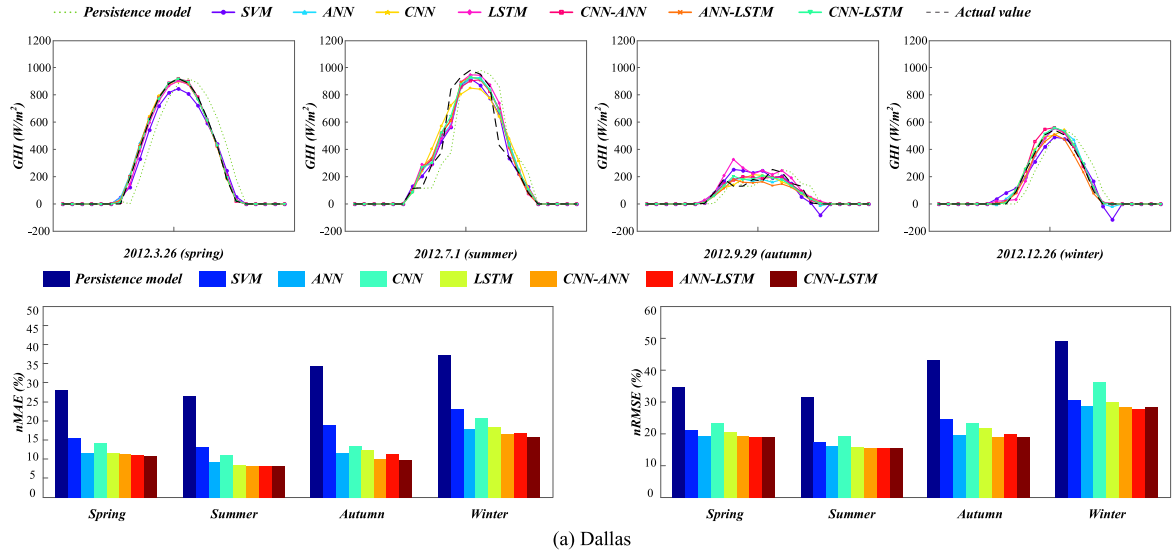
normalized prediction errors of spring and summer are similarly moderate and the prediction errors are slightly greater in autumn and greatest in winter. Moreover, it is once again noted that the performance improvement of the CNN-LSTM model is greater in autumn and winter when the prediction errors are greater. For example, the nMAE value of the CNN-LSTM model in summer is reduced by 0.16% compared with that of the CNN-ANN model and 0.07% compared with that of the ANN-LSTM model, while the nRMSE value of the CNN-LSTM model is reduced by 0.29% compared with that of the CNN-ANN model and 0.16% compared with that of the ANN-LSTM model. Meanwhile, the nMAE value of the CNN-LSTM model in autumn is reduced by 0.16% compared with that of the CNN-ANN model and 0.44% compared with that of the ANN-LSTM model, while the nRMSE value of the CNN-LSTM model is reduced by 0.41% compared with that of the CNN-ANN model and 0.46% compared with that of the ANN-LSTM model.

5.3. Performance under different sky conditions

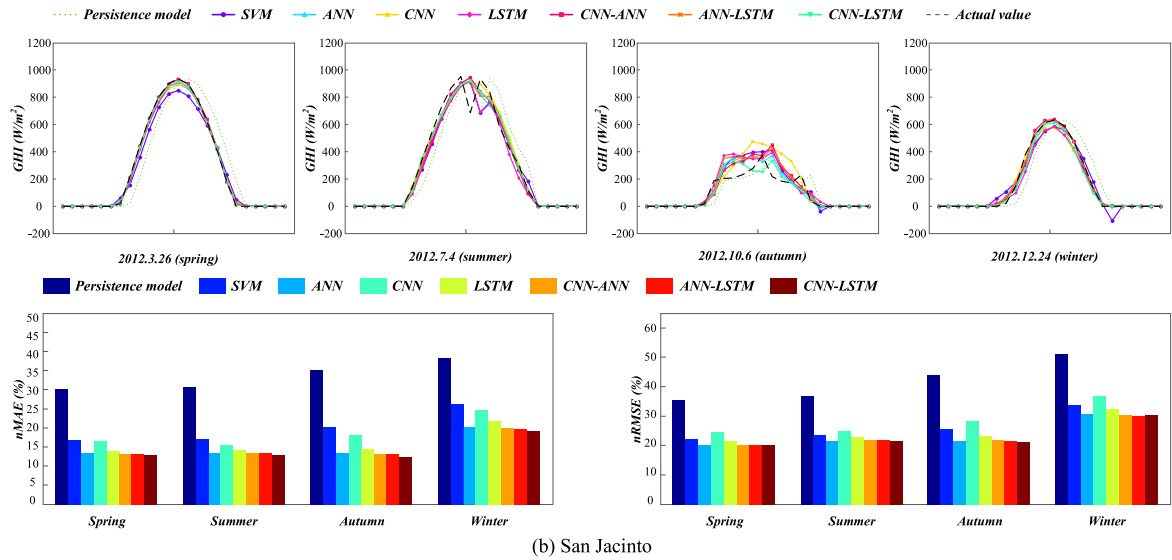
Clearness index (k_t) is a good proxy to sky condition. The percents of cloudy ($0 \leq k_t \leq 0.3$), partly cloudy ($0.3 < k_t \leq 0.7$) and cloudless ($0.7 < k_t \leq 1$) hours for each target site on the testing set are given in Table 5. According to the distribution of sky conditions for each site in Table 5, prediction results of eight models for five target sites under three different sky conditions are calculated and listed in Table 6, where the values given in bold represent the best performance metric values of all models. The number of times each model obtains the best performance metric values in terms of three

Table 4
Seasonal prediction results of the different models at the five target sites.

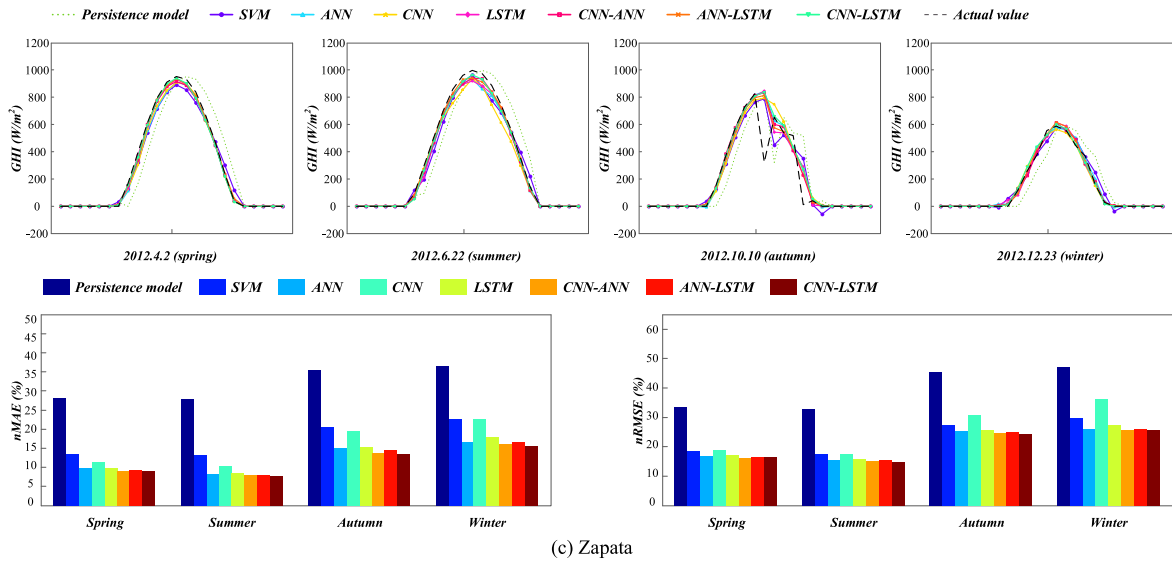
Season	Model	Dallas					San Jacinto					Zapata					Moore					Lamb				
		MAE	nMAE	RMSE	nRMSE	R	MAE	nMAE	RMSE	nRMSE	R	MAE	nMAE	RMSE	nRMSE	R	MAE	nMAE	RMSE	nRMSE	R	MAE	nMAE	RMSE	nRMSE	R
		(W/ m ²)	(%)	(W/ m ²)	(%)		(W/ m ²)	(%)	(W/ m ²)	(%)		(W/ m ²)	(%)	(W/ m ²)	(%)		(W/ m ²)	(%)	(W/ m ²)	(%)		(W/ m ²)	(%)	(W/ m ²)	(%)	
Spring	Persistence model	139.74	28.13	171.59	34.54	0.8539	146.55	29.99	174.58	35.73	0.8396	148.01	28.10	176.23	33.46	0.8491	145.23	27.26	172.80	32.44	0.8570	147.87	26.84	173.27	31.45	0.8609
	SVM	76.71	15.44	104.01	20.94	0.9493	81.61	16.70	108.20	22.15	0.9394	70.99	13.48	96.22	18.27	0.9561	75.42	14.16	100.56	18.88	0.9533	70.86	12.86	94.10	17.08	0.9617
	ANN	57.86	11.65	96.43	19.41	0.9533	65.15	13.34	98.91	20.24	0.9475	51.45	9.77	87.92	16.69	0.9619	54.76	10.28	93.38	17.53	0.9574	49.32	8.95	84.37	15.32	0.9667
	CNN	70.91	14.27	116.66	23.48	0.9302	80.03	16.38	120.03	24.57	0.9224	59.54	11.31	99.93	18.98	0.9503	67.41	12.66	118.00	22.15	0.9321	64.16	11.65	110.31	20.02	0.9426
	LSTM	57.92	11.66	101.42	20.41	0.9476	67.44	13.80	105.04	21.50	0.9402	51.96	9.87	91.03	17.29	0.9590	56.43	10.59	97.18	18.24	0.9537	50.16	9.11	87.79	15.94	0.9637
	CNN-ANN	56.23	11.32	96.00	19.32	0.9533	64.12	13.12	98.89	20.24	0.9473	47.17	8.96	85.05	16.15	0.9643	50.97	9.57	90.96	17.08	0.9596	48.09	8.73	83.75	15.20	0.9670
	ANN-LSTM	55.34	11.14	93.63	18.85	0.9556	64.18	13.14	98.70	20.20	0.9476	47.92	9.10	86.41	16.41	0.9632	51.10	9.59	92.65	17.39	0.9582	46.64	8.47	83.63	15.18	0.9673
	CNN-LSTM	54.11	10.89	94.95	19.11	0.9542	62.39	12.77	98.43	20.15	0.9478	47.73	9.06	85.83	16.30	0.9636	50.49	9.48	90.77	17.04	0.9598	46.65	8.47	84.06	15.26	0.9668
Summer	Persistence model	137.53	26.53	163.29	31.50	0.8623	147.30	30.78	177.13	37.02	0.8218	147.93	27.89	174.18	32.84	0.8525	143.18	26.03	164.67	29.94	0.8609	148.73	27.61	173.81	32.27	0.8511
	SVM	67.84	13.09	90.52	17.46	0.9615	82.21	17.18	112.70	23.55	0.9267	69.63	13.13	93.51	17.63	0.9594	61.21	11.13	81.56	14.83	0.9690	69.22	12.85	99.14	18.41	0.9529
	ANN	47.27	9.12	84.28	16.26	0.9629	64.73	13.53	103.47	21.62	0.9374	43.18	8.14	81.04	15.28	0.9676	42.18	7.67	68.74	12.50	0.9766	46.81	8.69	88.79	16.48	0.9605
	CNN	56.90	10.98	100.24	19.34	0.9467	73.57	15.37	118.34	24.73	0.9176	53.64	10.11	92.16	17.38	0.9578	50.27	9.14	86.47	15.72	0.9614	61.33	11.39	119.47	22.18	0.9282
	LSTM	43.49	8.39	81.81	15.78	0.9650	67.25	14.05	108.47	22.67	0.9311	44.70	8.43	84.15	15.87	0.9650	35.21	6.40	68.87	12.52	0.9756	44.57	8.27	91.14	16.92	0.9582
	CNN-ANN	42.74	8.25	80.43	15.52	0.9660	65.01	13.59	105.28	22.00	0.9350	41.96	7.91	80.45	15.17	0.9681	36.59	6.65	65.74	11.95	0.9778	45.09	8.37	89.16	16.55	0.9602
	ANN-LSTM	42.52	8.20	79.22	15.28	0.9671	64.73	13.53	103.99	21.73	0.9366	42.12	7.94	80.98	15.27	0.9677	35.02	6.37	64.76	11.77	0.9784	44.62	8.28	88.44	16.42	0.9609
	CNN-LSTM	41.96	8.09	80.41	15.51	0.9660	62.02	12.96	103.44	21.62	0.9374	40.35	7.61	78.30	14.76	0.9698	35.78	6.51	65.78	11.96	0.9777	44.21	8.21	87.61	16.26	0.9615
Autumn	Persistence model	101.66	34.50	127.59	43.31	0.8695	103.80	35.14	130.14	44.05	0.8697	110.62	35.33	141.91	45.32	0.8621	99.64	33.64	124.58	42.05	0.8751	105.21	33.38	130.17	41.30	0.8732
	SVM	55.55	18.85	71.87	24.39	0.9586	60.04	20.32	76.07	25.75	0.9553	63.81	20.38	86.26	27.55	0.9485	49.56	16.73	63.03	21.28	0.9683	48.95	15.53	63.67	20.20	0.9698
	ANN	34.21	11.61	57.68	19.58	0.9730	39.72	13.45	63.21	21.40	0.9688	46.73	14.92	78.58	25.10	0.9573	34.66	11.70	53.43	18.04	0.9769	29.89	9.48	52.01	16.50	0.9796
	CNN	39.55	13.42	68.98	23.41	0.9612	53.16	17.99	83.44	28.25	0.9450	60.45	19.30	95.94	30.64	0.9355	41.61	14.05	68.14	23.00	0.9620	36.22	11.49	60.67	19.25	0.9725
	LSTM	36.58	12.42	63.92	21.69	0.9668	42.50	14.39	68.07	23.04	0.9639	47.18	15.07	80.09	25.58	0.9551	31.90	10.77	53.76	18.15	0.9765	29.14	9.25	53.48	16.97	0.9784
	CNN-ANN	29.61	10.05	55.87	18.96	0.9747	39.10	13.24	64.30	21.76	0.9678	43.00	13.73	76.43	24.41	0.9596	29.20	9.86	51.46	17.37	0.9785	25.77	8.17	49.41	15.68	0.9816
	ANN-LSTM	33.20	11.27	58.68	19.92	0.9721	39.19	13.27	63.58	21.52	0.9685	45.48	14.52	77.65	24.80	0.9583	29.11	9.83	52.11	17.59	0.9779	26.64	8.45	49.57	15.73	0.9814
	CNN-LSTM	28.75	9.76	56.14	19.05	0.9745	36.31	12.29	62.36	21.11	0.9697	41.98	13.41	75.72	24.18	0.9605	28.03	9.46	50.72	17.12	0.9791	25.24	8.01	48.13	15.27	0.9825
Winter	Persistence model	99.03	37.27	130.44	49.09	0.8575	92.97	38.45	123.19	50.95	0.8598	103.74	36.31	134.59	47.10	0.8637	98.48	34.67	128.02	45.07	0.8725	101.67	32.96	130.16	42.19	0.8815
	SVM	61.15	23.01	81.49	30.67	0.9435	63.47	26.25	81.73	33.80	0.9369	64.73	22.65	84.17	29.46	0.9456	56.46	19.88	74.64	26.28	0.9570	56.08	18.18	71.34	23.13	0.9665
	ANN	47.40	17.84	76.33	28.73	0.9505	48.79	20.18	74.13	30.66	0.9481	47.39	16.58	74.18	25.96	0.9581	42.99	15.14	66.95	23.57	0.9646	36.88	11.96	58.62	19.00	0.9758
	CNN	55.08	20.73	95.57	35.97	0.9220	60.01	24.82	89.31	36.94	0.9248	64.63	22.62	103.17	36.11	0.9188	48.84	17.20	80.59	28.37	0.9483	46.75	15.16	77.65	25.17	0.9571
	LSTM	48.58	18.28	79.31	29.85	0.9460	52.32	21.64	78.56	32.49	0.9415	51.20	17.92	78.04	27.31	0.9534	40.25	14.17	69.91	24.61	0.9613	35.67	11.56	61.38	19.90	0.9734
	CNN-ANN	43.90	16.52	75.51	28.42	0.9516	48.24	19.95	73.08	30.23	0.9496	45.94	16.08	73.52	25.73	0.9587	36.00	12.67	64.18	22.59	0.9675	31.96	10.36	55.47	17.98	0.9782
	ANN-LSTM	44.58	16.78	73.55	27.68	0.9540	48.06	19.88	72.49	29.98	0.9505	46.83	16.39	74.10	25.93	0.9582	36.44	12.83	63.05	22.20	0.9686	32.99	10.69	56.78	18.41	0.9772
	CNN-LSTM	42.31	15.92	75.49	28.41	0.9516	46.57	19.26	73.17	30.26	0.9495	44.55	15.59	73.29	25.65	0.9588	34.35	12.09	62.87	22.14	0.9688	32.16	10.42	57.51	18.64	0.9766



(a) Dallas



(b) San Jacinto



(c) Zapata

Fig. 9. Seasonal GHI distribution curves and the normalized evaluation metric values obtained by the different models at the five target sites.

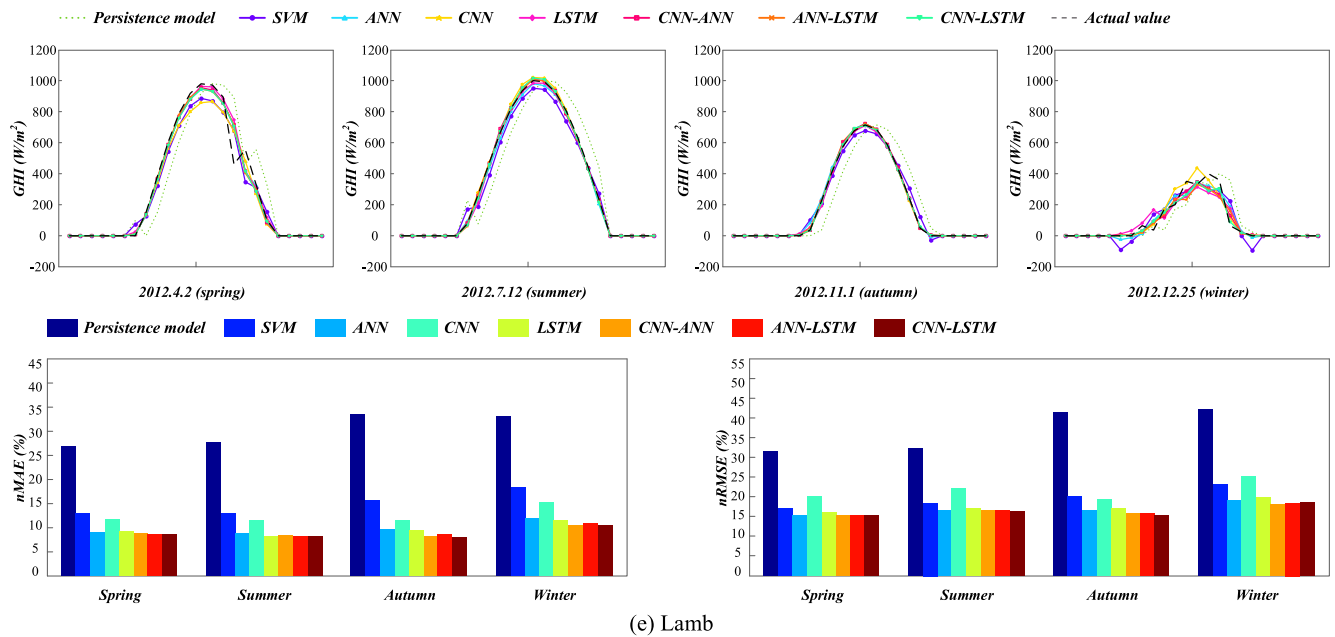
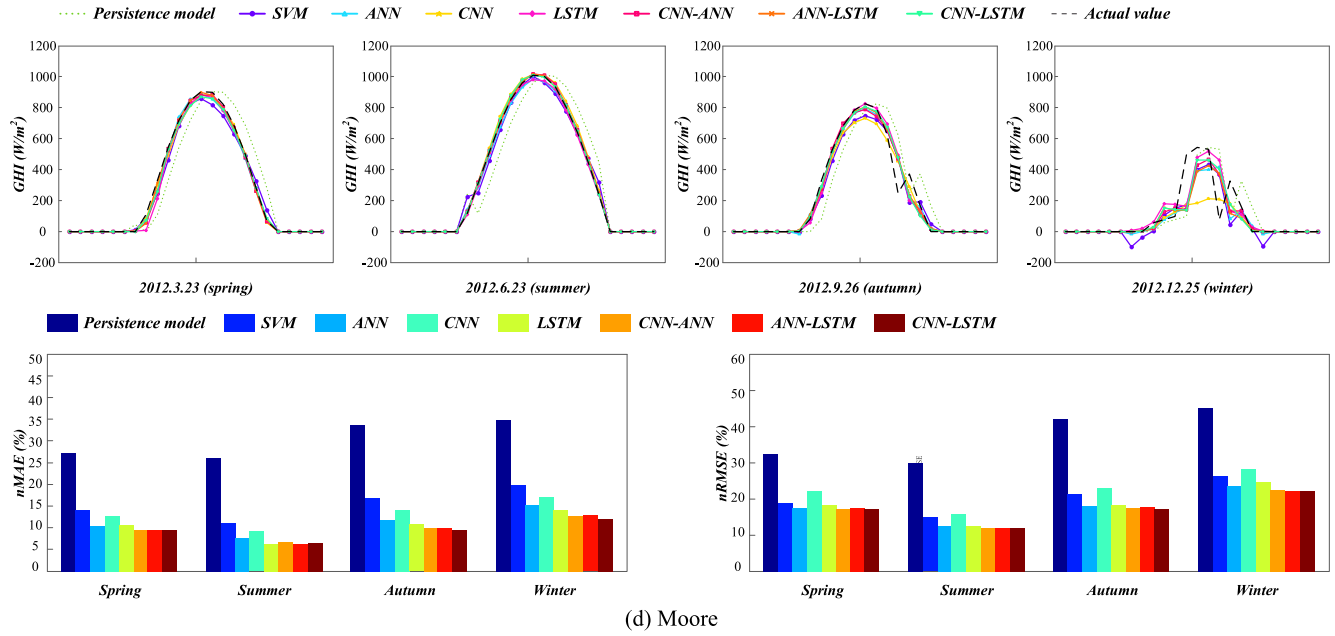


Fig. 9. (continued).

sky conditions is shown in Fig. 10.

For cloudy sky conditions, various models obtain the best performance metric values according to the Table 6 and Fig. 10. Meanwhile, the CNN-LSTM model performs best in 9 of total 25 cases. For instance, the MAE and nMAE values of CNN-LSTM are best in Zapata and the values are 44.56 W/m² and 145.02 W/m² respectively. This number 9 is highest of all models, demonstrating the superiority of the proposed hybrid model under cloudy sky conditions.

When the sky condition is partly cloudy, the SVM model achieves the best prediction performances in most cases according to Table 6 and Fig. 10. Although the CNN-LSTM model only performs best in 4 of total 25 cases, the prediction performance of the proposed model is also good in the remaining cases.

Under cloudless sky conditions, the CNN-LSTM model performs best in 17 of total 25 cases and this number is the highest of all eight models as well. For instance, the CNN-LSTM model owns the best prediction results of all eight models regardless of the performance evaluation metrics in San Jacinto and Moore. The MAE, nMAE, RMSE, nRMSE and R values of CNN-LSTM in San Jacinto are 44.26 W/m², 8.91%, 69.86 W/m², 14.07% and 0.9734 respectively, and the MAE, nMAE, RMSE, nRMSE and R values of CNN-LSTM in Moore are 30.50 W/m², 5.76%, 50.95 W/m², 9.62% and 0.9854 respectively, indicating the good prediction performance of the proposed hybrid model.

Table 5

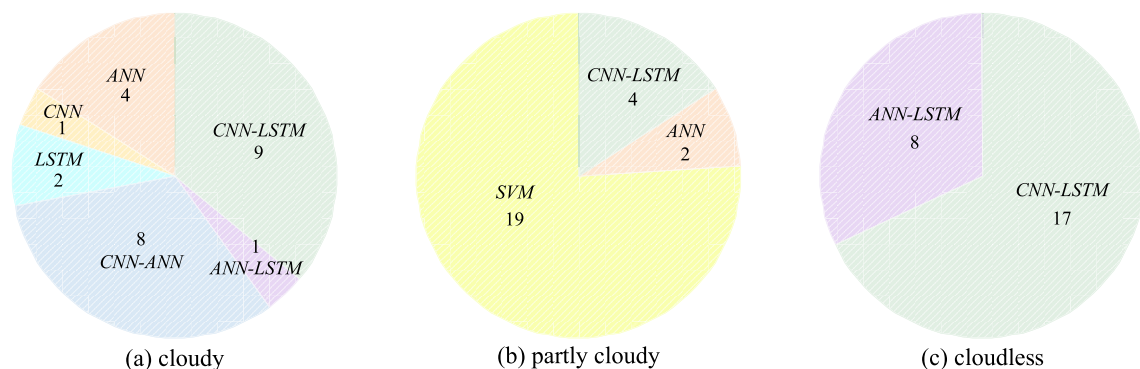
The percents of cloudy, partly cloudy and cloudless hours for each target site on the testing set.

Site	$0 \leq k_t \leq 0.3$ (cloudy)	$0.3 < k_t \leq 0.7$ (partly cloudy)	$0.7 < k_t \leq 1$ (cloudless)
Dallas	797h (16.75%)	635h (13.35%)	3326h (69.90%)
San Jacinto	849h (17.84%)	781h (16.41%)	3128h (65.74%)
Zapata	667h (14.02%)	732h (15.38%)	3359h (70.60%)
Moore	704h (14.80%)	590h (12.40%)	3464h (72.80%)
Lamb	688h (14.46%)	522h (10.97%)	3548h (74.57%)

Table 6

Prediction results of different models under three sky conditions.

Site	Model	$0 \leq k_t \leq 0.3$ (cloudy)					$0.3 < k_t \leq 0.7$ (partly cloudy)					$0.7 < k_t \leq 1$ (cloudless)				
		MAE (W/m ²)	nMAE (%)	RMSE (W/m ²)	nRMSE (%)	R	MAE (W/m ²)	nMAE (%)	RMSE (W/m ²)	nRMSE (%)	R	MAE (W/m ²)	nMAE (%)	RMSE (W/m ²)	nRMSE (%)	R
Dallas	Persistence model	55.69	172.88	106.14	329.52	0.6185	120.25	48.91	158.19	64.34	0.6370	135.08	26.41	156.94	30.68	0.8500
	SVM	71.02	220.49	106.76	331.46	0.8282	81.42	33.11	109.89	44.69	0.8394	61.03	11.93	77.63	15.18	0.9711
	ANN	54.48	169.15	102.08	316.91	0.8374	90.25	36.70	122.73	49.91	0.8058	36.63	7.16	61.72	12.07	0.9782
	CNN	52.27	162.28	119.16	369.94	0.8309	112.13	45.60	152.59	62.06	0.7660	45.82	8.96	75.09	14.68	0.9702
	LSTM	54.63	169.62	106.45	330.48	0.8194	88.70	36.08	125.18	50.91	0.8129	36.80	7.19	64.15	12.54	0.9775
	CNN-ANN	41.46	128.71	97.94	304.07	0.8204	87.86	35.73	123.61	50.27	0.8127	35.13	6.87	59.91	11.71	0.9804
	ANN-LSTM	46.35	143.90	99.35	308.46	0.8297	87.66	35.65	120.93	49.18	0.8258	35.09	6.86	58.52	11.44	0.9813
	CNN-LSTM	41.62	129.21	99.58	309.17	0.8213	87.64	35.65	122.84	49.96	0.8155	33.21	6.49	59.02	11.54	0.9807
San Jacinto	Persistence model	63.26	156.41	114.68	283.55	0.6434	125.66	46.78	160.99	59.93	0.7301	138.63	27.91	160.87	32.39	0.8395
	SVM	79.59	196.79	114.06	282.02	0.8478	82.67	30.77	112.35	41.82	0.8800	67.27	13.54	86.11	17.34	0.9633
	ANN	56.64	140.03	103.50	255.91	0.8385	84.24	31.36	118.25	44.02	0.8725	46.90	9.44	71.21	14.34	0.9725
	CNN	66.88	165.35	126.85	313.63	0.8427	97.23	36.20	134.33	50.01	0.8401	59.27	11.93	87.73	17.66	0.9602
	LSTM	61.07	150.99	112.50	278.15	0.8308	89.40	33.28	123.52	45.98	0.8662	48.63	9.79	74.90	15.08	0.9696
	CNN-ANN	53.37	131.95	106.16	262.48	0.8432	83.48	31.08	118.00	43.93	0.8762	47.25	9.51	71.22	14.34	0.9721
	ANN-LSTM	54.37	134.43	104.26	257.78	0.8445	83.41	31.05	117.62	43.79	0.8775	46.88	9.44	70.83	14.26	0.9728
	CNN-LSTM	52.06	128.71	104.41	258.16	0.8483	82.93	30.87	118.36	44.06	0.8744	44.26	8.91	69.86	14.07	0.9734
Zapata	Persistence model	51.73	168.34	107.06	348.40	0.5932	127.11	48.94	164.22	63.23	0.6767	143.21	27.21	165.14	31.37	0.8479
	SVM	73.20	238.22	109.92	357.71	0.8629	86.51	33.31	118.53	45.64	0.8676	61.99	11.78	77.96	14.81	0.9725
	ANN	52.09	169.51	100.99	328.64	0.8570	93.92	36.16	132.68	51.09	0.8704	36.03	6.85	57.90	11.00	0.9836
	CNN	61.30	199.49	125.54	408.56	0.8709	121.88	46.93	161.65	62.24	0.8562	45.57	8.66	68.86	13.08	0.9776
	LSTM	51.87	168.78	102.06	332.12	0.8273	92.47	35.61	130.72	50.33	0.8385	38.61	7.34	63.99	12.16	0.9796
	CNN-ANN	46.07	149.92	96.86	315.22	0.8551	92.53	35.63	130.88	50.40	0.8582	33.75	6.41	57.04	10.84	0.9833
	ANN-LSTM	48.96	159.33	99.62	324.20	0.8593	94.71	36.47	132.79	51.13	0.8573	34.20	6.50	56.99	10.83	0.9832
	CNN-LSTM	44.56	145.02	97.16	316.18	0.8478	90.96	35.02	130.03	50.07	0.8598	33.17	6.30	56.28	10.69	0.9838
Moore	Persistence model	51.93	247.92	104.12	497.11	0.5797	121.14	51.79	158.18	67.62	0.7011	136.39	25.74	155.56	29.36	0.8542
	SVM	66.39	317.00	100.82	481.36	0.8291	82.52	35.28	112.61	48.14	0.8756	55.95	10.56	69.64	13.15	0.9766
	ANN	49.70	237.27	92.19	440.17	0.8429	85.00	36.34	120.82	51.65	0.8777	35.48	6.70	54.38	10.26	0.9837
	CNN	48.06	229.45	118.96	567.99	0.8418	111.57	47.70	159.01	67.98	0.8627	42.86	8.09	63.62	12.01	0.9782
	LSTM	42.51	202.98	92.93	443.71	0.8112	83.45	35.68	121.73	52.04	0.8664	33.50	6.32	57.44	10.84	0.9816
	CNN-ANN	34.49	164.66	85.33	407.39	0.8397	81.57	34.87	120.60	51.56	0.8737	31.68	5.98	52.20	9.85	0.9848
	ANN-LSTM	34.98	167.01	87.24	416.53	0.8362	83.91	35.87	122.07	52.19	0.8728	30.80	5.81	51.33	9.69	0.9851
	CNN-LSTM	34.45	164.48	88.02	420.25	0.8401	80.28	34.32	119.19	50.95	0.8757	30.50	5.76	50.95	9.62	0.9854
Lamb	Persistence model	51.60	187.64	100.14	364.18	0.6727	131.31	54.64	172.49	71.78	0.7003	139.97	26.10	159.30	29.71	0.8507
	SVM	70.06	254.78	106.22	386.28	0.8974	89.63	37.30	124.78	51.93	0.8762	55.59	10.37	70.02	13.06	0.9780
	ANN	49.01	178.23	100.04	363.84	0.8959	91.85	38.22	133.22	55.44	0.8705	31.76	5.92	50.85	9.48	0.9861
	CNN	55.63	202.32	140.48	510.91	0.8712	124.64	51.87	178.34	74.22	0.8423	41.00	7.65	60.87	11.35	0.9806
	LSTM	46.01	167.34	97.64	355.11	0.8844	90.99	37.86	134.98	56.17	0.8619	31.35	5.85	55.79	10.40	0.9831
	CNN-ANN	42.12	153.17	100.64	365.99	0.8895	89.82	37.38	134.39	55.93	0.8727	29.40	5.48	47.93	8.94	0.9875
	ANN-LSTM	44.63	162.31	102.76	373.71	0.9020	91.69	38.16	135.67	56.46	0.8728	28.61	5.34	46.54	8.68	0.9882
	CNN-LSTM	40.37	146.80	97.99	356.38	0.8929	88.82	36.96	133.83	55.69	0.8729	28.99	5.41	48.79	9.10	0.9872

**Fig. 10.** The number of times each model obtains the best performance metric values in terms of three sky conditions.

6. Conclusion

This study proposes a hybrid CNN-LSTM model with spatio-temporal correlations to improve the accuracy of short-term solar radiation prediction for supporting the optimum dispatch and management of power systems with high penetrations of PV power generation. The proposed model adopts a CNN to extract spatial features based on meteorological parameters and an LSTM network to extract temporal features based on historical GHI time series data, and effectively combines the temporal and spatial correlations of the data to obtain accurate GHI predictions 1 h in advance. The prediction performance and generalization ability of the proposed hybrid CNN-LSTM model are rigorously evaluated by analyzing its GHI prediction results in a whole year, different seasons and different sky conditions when applied to three datasets composed of spatiotemporal data collected from 34 locations spread across three different climate zones in Texas, USA. Meanwhile, the prediction performance of the CNN-LSTM model is compared with the performances obtained using the persistence model, SVM, ANN, CNN, LSTM, CNN-ANN, and ANN-LSTM models based on five evaluation metrics. The prediction results indicate that the proposed model typically provides the best annual and seasonal prediction performances of all models considered at the five target sites of the three datasets. The MAE values of CNN-LSTM at Dallas, San Jacinto, Zapata, Moore and Lamb on the whole year dataset are 41.88 W/m², 52.00 W/m², 43.66 W/m², 37.26 W/m² and 37.20 W/m², respectively. The percentile improvements at five target sites are 3.10%, 4.22%, 1.93%, 2.66% and 1.77% compared with CNN-ANN and 4.80%, 4.08%, 4.21%, 1.95% and 1.72% compared with ANN-LSTM, demonstrating the superiority of combining spatial and temporal correlations by means of the CNN-LSTM model. Meanwhile, the seasonal prediction results demonstrate that the seasonal distribution of prediction errors changes with respect to climate, and that the proposed CNN-LSTM model provides prediction results that are more greatly improved relative to the results of the other models considered during seasons when the prediction errors are relatively large. In addition, the proposed model has more improvement in cloudy and cloudless sky conditions, and a slight advance in partly cloudy sky condition according to the prediction results. The proposed hybrid model is hereby demonstrated to be a good choice for short-term GHI prediction, especially in cloudy and cloudless sky conditions. Meanwhile, the model needs massive data and has many parameters, so the training time is long. Therefore, storage and computing devices (such as GPU) are needed. In future research, the proposed model will be considered for long-term solar radiation prediction. Furthermore, other spatiotemporal correlation models are also worthy of further study.

CRedit authorship contribution statement

Haixiang Zang: Conceptualization, Methodology, Software. **Ling Liu:** Data curation, Software, Writing - original draft. **Li Sun:** Software, Writing - review & editing. **Lilin Cheng:** Writing - review & editing. **Zhinong Wei:** Writing - review & editing. **Guoqiang Sun:** Writing - review & editing.

Acknowledgements

The research is supported by National Natural Science Foundation of China (Program No. 51507052), the Fundamental Research Funds for the Central Universities (Program No. 2018B15414) and the Open Research Fund of Jiangsu Collaborative Innovation Center for Smart Distribution Network, Nanjing Institute of Technology (No. XTCX201812).

References

- [1] J.Y. Zhang, L. Zhao, S. Deng, W.C. Xu, Y. Zhang, A critical review of the models used to estimate solar radiation, *Renew. Sustain. Energy Rev.* 70 (2017) 314–329.
- [2] Z.F. Tan, H.J. Zhang, J. Xu, J.H. Wang, C. Yu, J.L. Zhang, Photovoltaic power generation in China: development potential, benefits of energy conservation and emission reduction, *J. Energy Eng-Asce* 138 (2) (2012) 73–86.
- [3] G. Farivar, B. Asaei, A new approach for solar module temperature estimation using the simple diode model, *IEEE Trans. Energy Convers.* 26 (4) (2011) 1118–1126.
- [4] R. Perez, T. Hoff, J. Dize, D. Chalmers, S. Kivalov, The cost of mitigating short-term PV output variability, *Energy Proced.* 57 (2014), 755–+.
- [5] E.S. Mostafaei, S.S. Ramiyani, R. Sarvar, H.I. Moud, S.M. Mousavi, A hybrid computational approach to estimate solar global radiation: an empirical evidence from Iran, *Energy* 49 (2013) 204–210.
- [6] M. Diagne, M. David, P. Lauret, J. Boland, N. Schmutz, Review of solar irradiance forecasting methods and a proposition for small-scale insular grids, *Renew. Sustain. Energy Rev.* 27 (2013) 65–76.
- [7] R.H. Inman, H.T.C. Pedro, C.F.M. Coimbra, Solar forecasting methods for renewable energy integration, *Prog. Energy Combust.* 39 (6) (2013) 535–576.
- [8] T. Khatib, A. Mohamed, K. Sopian, A review of solar energy modeling techniques, *Renew. Sustain. Energy Rev.* 16 (5) (2012) 2864–2869.
- [9] J. Widen, N. Carpmann, V. Castellucci, D. Lingfors, J. Olsson, F. Remouit, M. Bergkvist, M. Grabbe, R. Waters, Variability assessment and forecasting of renewables: a review for solar, wind, wave and tidal resources, *Renew. Sustain. Energy Rev.* 44 (2015) 356–375.
- [10] S. Alessandrini, L. Delle Monache, S. Sperati, G. Cervone, An analog ensemble for short-term probabilistic solar power forecast, *Appl. Energy* 157 (2015) 95–110.
- [11] L. Nonnenmacher, A. Kaur, C.F.M. Coimbra, Day-ahead resource forecasting for concentrated solar power integration, *Renew. Energy* 86 (2016) 866–876.
- [12] R. Perez, S. Kivalov, J. Schlemmer, K. Hemker, D. Renne, T.E. Hoff, Validation of short and medium term operational solar radiation forecasts in the US, *Sol. Energy* 84 (12) (2010) 2161–2172.
- [13] R. Marquez, C.F.M. Coimbra, Intra-hour DNI forecasting based on cloud tracking image analysis, *Sol. Energy* 91 (2013) 327–336.
- [14] A. Ahmad, T.N. Anderson, T.T. Lie, Hourly global solar irradiation forecasting for New Zealand, *Sol. Energy* 122 (2015) 1398–1408.
- [15] J. Huang, M. Korolkiewicz, M. Agrawal, J. Boland, Forecasting solar radiation on an hourly time scale using a Coupled AutoRegressive and Dynamical System (CARDS) model, *Sol. Energy* 87 (2013) 136–149.
- [16] J.C. Cao, X.C. Lin, Application of the diagonal recurrent wavelet neural network to solar irradiation forecast assisted with fuzzy technique, *Eng. Appl. Artif. Intell.* 21 (8) (2008) 1255–1263.
- [17] J. Wu, C.K. Chan, Prediction of hourly solar radiation using a novel hybrid model of ARMA and TDNN, *Sol. Energy* 85 (5) (2011) 808–817.
- [18] R. Marquez, H.T.C. Pedro, C.F.M. Coimbra, Hybrid solar forecasting method uses satellite imaging and ground telemetry as inputs to ANNs, *Sol. Energy* 92 (2013) 176–188.
- [19] A. Mellit, M. Benghanem, A.H. Arab, A. Guessoum, A simplified model for generating sequences of global solar radiation data for isolated sites: using artificial neural network and a library of Markov transition matrices approach, *Sol. Energy* 79 (5) (2005) 469–482.
- [20] R. Perez, E. Lorenz, S. Pelland, M. Beauharnois, G. Van Knowe, K. Hemker, D. Heinemann, J. Remund, S.C. Muller, W. Traunmuller, G. Steinmauer, D. Pozo, J.A. Ruiz-Arias, V. Lara-Fanego, L. Ramirez-Santigosa, M. Gaston-Romero, L.M. Pomares, Comparison of numerical weather prediction solar irradiance forecasts in the US, Canada and Europe, *Sol. Energy* 94 (2013) 305–326.
- [21] G.M. Yaghi, D.Z. Yang, D. Srinivasan, Automatic hourly solar forecasting using machine learning models, *Renew. Sustain. Energy Rev.* 105 (2019) 487–498.
- [22] P. Mathiesen, J. Kleissl, Evaluation of numerical weather prediction for intraday solar forecasting in the continental United States, *Sol. Energy* 85 (5) (2011) 967–977.
- [23] Y. Chen, S. Zhang, W.Y. Zhang, J.J. Peng, Y.S. Cai, Multifactor spatio-temporal correlation model based on a combination of convolutional neural network and long short-term memory neural network for wind speed forecasting, *Energy Convers. Manag.* 185 (2019) 783–799.
- [24] J.L. Bosch, Y. Zheng, J. Kleissl, Deriving cloud velocity from an array of solar radiation measurements, *Sol. Energy* 87 (2013) 196–203.
- [25] H. Bouzgou, C.A. Gueymard, Fast short-term global solar irradiance forecasting with wrapper mutual information, *Renew. Energy* 133 (2019) 1055–1065.
- [26] G. Reikard, Predicting solar radiation at high resolutions: a comparison of time series forecasts, *Sol. Energy* 83 (3) (2009) 342–349.
- [27] C. Voyant, G. Notton, S. Kalogiou, M.L. Nivet, C. Paoli, F. Motte, A. Fouilloy, Machine learning methods for solar radiation forecasting: a review, *Renew. Energy* 105 (2017) 569–582.
- [28] F.V. Gutierrez-Corea, M.A. Manso-Callejo, M.P. Moreno-Regidor, M.T. Manrique-Sancho, Forecasting short-term solar irradiance based on artificial neural networks and data from neighboring meteorological stations, *Sol. Energy* 134 (2016) 119–131.
- [29] P. Lauret, C. Voyant, T. Soubdhan, M. David, P. Poggi, A benchmarking of machine learning techniques for solar radiation forecasting in an insular context, *Sol. Energy* 112 (2015) 446–457.

- [30] A. Mellit, A.M. Pavan, A 24-h forecast of solar irradiance using artificial neural network: application for performance prediction of a grid-connected PV plant at Trieste, Italy, *Sol. Energy* 84 (5) (2010) 807–821.
- [31] C.J. Huang, P.H. Kuo, Multiple-input deep convolutional neural network model for short-term photovoltaic power forecasting, *IEEE Access* 7 (2019) 74822–74834.
- [32] S. Ghimire, R.C. Deo, N. Raj, J.C. Mi, Deep learning neural networks trained with MODIS satellite-derived predictors for long-term global solar radiation prediction, *Energies* 12 (12) (2019).
- [33] K. Kaba, M. Sarigul, M. Avci, H.M. Kandirmaz, Estimation of daily global solar radiation using deep learning model, *Energy* 162 (2018) 126–135.
- [34] J. Lago, K. De Brabandere, F. De Ridder, B. De Schutter, Short-term forecasting of solar irradiance without local telemetry: a generalized model using satellite data, *Sol. Energy* 173 (2018) 566–577.
- [35] A. Moncada, W. Richardson, R. Vega-Avila, Deep learning to forecast solar irradiance using a six-month UTSA SkylImager dataset, *Energies* 11 (8) (2018).
- [36] X.Y. Qing, Y.G. Niu, Hourly day-ahead solar irradiance prediction using weather forecasts by LSTM, *Energy* 148 (2018) 461–468.
- [37] S. Srivastava, S. Lessmann, A comparative study of LSTM neural networks in forecasting day-ahead global horizontal irradiance with satellite data, *Sol. Energy* 162 (2018) 232–247.
- [38] H.X. Zang, L.L. Cheng, T. Ding, K.W. Cheung, M.M. Wang, Z.N. Wei, G.Q. Sun, Application of functional deep belief network for estimating daily global solar radiation: a case study in China, *Energy* 191 (2020).
- [39] L. Ye, Z.G. Cao, Y. Xiao, DeepCloud: ground-based cloud image categorization using deep convolutional features, *IEEE T Geosci Remote* 55 (10) (2017) 5729–5740.
- [40] F. Rubel, K. Brugger, K. Haslinger, I. Auer, The climate of the European Alps: shift of very high resolution Koppen-Geiger climate zones 1800–2100, *Meteorol. Z.* 26 (2) (2017) 115–125.
- [41] M. Sengupta, Y. Xie, A. Lopez, A. Habte, G. Maclaurin, J. Shelby, The national solar radiation data Base (NSRDB), *Renew. Sustain. Energy Rev.* 89 (2018) 51–60.
- [42] Y. LeCun, B. Boser, J.S. Denker, D. Henderson, R.E. Howard, W. Hubbard, L.D. Jackel, Backpropagation applied to Handwritten Zip Code Recognition 1 (4) (1989) 541–551.
- [43] Y. Ju, G.Y. Sun, Q.H. Chen, M. Zhang, H.X. Zhu, M.U. Rehman, A model combining convolutional neural network and LightGBM algorithm for ultra-short-term wind power forecasting, *IEEE Access* 7 (2019) 28309–28318.
- [44] S.W. Ji, W. Xu, M. Yang, K. Yu, 3D convolutional neural networks for human action recognition, *IEEE T Pattern Anal* 35 (1) (2013) 221–231.
- [45] H. Liu, X.W. Mi, Y.F. Li, Wind speed forecasting method based on deep learning strategy using empirical wavelet transform, long short term memory neural network and Elman neural network, *Energy Convers. Manag.* 156 (2018) 498–514.
- [46] H. Liu, X.W. Mi, Y.F. Li, Smart multi-step deep learning model for wind speed forecasting based on variational mode decomposition, singular spectrum analysis, LSTM network and ELM, *Energy Convers. Manag.* 159 (2018) 54–64.
- [47] L. Benali, G. Notton, A. Fouilloy, C. Voyant, R. Dizene, Solar radiation forecasting using artificial neural network and random forest methods: application to normal beam, horizontal diffuse and global components, *Renew. Energy* 132 (2019) 871–884.